Nano World Journal

https://doi.org/10.17756/nwj.2023-s3-122

Research Article

Open Access

Optimizing the Fracture Behavior of Zirconia-Graphene Nanocomposites Through Advanced Shear-lag Modeling

Ibrokhim.B.Sapaev[1], L.H. Jasim[2*], Mahalakshmi[3], Subramani Rajamanickam[4], Venkata Subramani[5] and Vivek Veeman[6]

[1]Tashkent Institute of Irrigation and Agricultural Mechanization Engineers" National Research University, Tashkent, Uzbekistan, Head of the department «Physics and Chemistry, School of Engineering, Central Asian University, Tashkent, Uzbekistan

[2]College of Technical Engineering, The Islamic University, Najaf, Iraq

[3]Department of Electrical and Electronics Engineering, Prince Shri Venkateshwara Padmavathy Engineering College, Chennai, Tamil Nadu, India

[4]Department of Mathematics, Christ (Deemed to be University), Bengaluru, Karnataka, India

[5]Department of Electronics and Communication Engineering, New Prince Shri Bhavani College of Engineering, Chennai, Tamil Nadu, India

[6]Department of Computer Science and Engineering, AAA College of Engineering and Technology, Sivakasi, Tamil Nadu, India

[*]Correspondence to:
L.H. Jasim
College of Technical Engineering,
The Islamic University,
Najaf, Iraq.
E-mail: dr.laith.h.alzubaidi@gmail.com

Received: July 28, 2023
Accepted: October 27, 2023
Published: October 31, 2023

Citation: Sapaev IB, Jasim LH, Mahalakshmi, Rajamanickam S, Subramani V, et al. 2023. Optimizing the Fracture Behavior of Zirconia-Graphene Nanocomposites Through Advanced Shear-lag Modeling. *NanoWorld J* 9(S3): S677-S684.

Copyright: © 2023 Sapaev et al. This is an Open Access article distributed under the terms of the Creative Commons Attribution 4.0 International License (CCBY) (http://creativecommons.org/licenses/by/4.0/) which permits commercial use, including reproduction, adaptation, and distribution of the article provided the original author and source are credited.

Published by United Scientific Group

Abstract

Graphene nanomaterial-reinforced zirconia matrix composites (ZMCs) have demonstrated exceptional load-carrying capabilities, even in the demanding conditions demanded by new applications. The main reason for their outstanding mechanical performance, particularly their resilience to cracks, is the diversity of their microstructures. Composites using intentionally scattered graphene exhibit exceptional resilience to catastrophic failure due to toughening mechanisms external to the matrix. Our investigation of the fractured behavior of these nanocomposites is insufficient, and the complex energy dissipation mechanism at the interface between the reinforcement and the matrix is hindering our progress in creating more robust and tougher ZMCs. To overcome these constraints, we study energy dissipation and fracture deflection in nanocomposites using an enhanced cohesive shear-lag approach. Nanocomposites' toughening is controlled by interfacial debonding and friction, which are taken into consideration in this novel model. Our study will inform you how to maximize the toughening effects of ZMCs.

Keywords

Graphene nanomaterials, Fracture toughness, Zirconia matrix composites, Failure criteria, Micromechanics, Mechanical properties of materials

Introduction

All materials, whether they are man-made or found in nature, exhibit some degree of microstructural variability. Natural and manufactured materials alike can attain mechanical characteristics and functions that surpass those of their constituent components through precise management of their heterogeneous microstructures [1-4]. As an example, high-performance ZMCs have garnered a lot of attention from researchers because of the demanding conditions they could be used in. These composites have the ability to withstand extreme heat and chemicals, making them ideal for use in energy storage systems and other harsh environments [5, 6]. The distinctive heterogeneous microstructure of these materials is made up of reinforcements that are finely dispersed throughout the zirconia matrix. The composites are robust enough to withstand catastrophic breakdown under different operating settings because these reinforcements allow toughening mechanisms that are not intrinsic to the zirconia matrix [7, 8]. In contrast, monolithic zirconia's aren't very trustworthy structural materials due to their low fracture toughness. To that end, one of the primary goals in developing ZMCs is to control the toughening effects.

In general, three parameters should determine the toughening effects in ZMCs from a microstructural standpoint. Matrix material and reinforcement selection is the primary consideration. Silicon carbide, carbon, silicon nitride, and aluminum oxide are common chemical compositions, and reinforcements can be in the form of particles, short fibers, long fibers, or sheets. The positioning of the matrix's reinforcements is the second consideration. Reinforcements can have an aligned or random orientation and a homogenous or inhomogeneous distribution. Interfaces between reinforcements and matrices constitute the third component. Various ZMCs, with different chemical compositions and production processes, can have different mechanical properties at the matrix/reinforcement contact. This means that ZMC toughening effects can be fine-tuned in a wide variety of ways. At least on a laboratory basis, all of the aforementioned factors have already been investigated experimentally. The incorporation of nanoparticles into composites has introduced a novel aspect—the reduction in reinforcement size—that has received little attention but might be a way to boost the toughening effects of ZMCs.

Based on graphene nanomaterial-reinforced composites as a scaled-down example, we investigate the mechanics of microfiber-reinforced composites in this study. When it comes to the predictions for reinforcement-induced toughening and the circumstances for crack deflection, our present knowledge of the fracture behaviour of these composites reinforced with graphene nanomaterial is lacking. For future research to make full use of nano-sized reinforcements, basic investigations on these two fronts are necessary. In addition, we dissect the unique reinforcements' defining characteristics as they pertain to graphene nanomaterials (such as graphene, reduced graphene oxide, and hexagonal boron nitride platelets). Graphene nanomaterial-reinforced zirconia composites can be optimized in terms of fracture toughness as a final result.

Methodology

Toughening in fiber-reinforced composites

When the concepts of fracture mechanics in homogeneous brittle materials were well established in the 1960s, researchers began investigating fracture in fiber-reinforced composites. The process by which embedded fibers toughen a composite material has been the subject of much research over the years. Of particular interest are two basic questions: (1) what kind of failure can occur near a fiber reinforcement, and (2) how can the contribution of reinforcements to fracture toughness be predicted? Because it is most pertinent to ZMCs, we pay zero attention on the particular mix of brittle fiber reinforcements and a brittle matrix here.

The first question has been thoroughly researched in the literature [9]. In this case, a large matrix crack runs into a series of fiber reinforcements. The greatest way to stop a running crack is to have a weak matrix/reinforcement contact that is perpendicular to the crack. By spreading the substantial near-tip stress over an interface—which can easily open or shear—placed knowingly in front of a matrix crack, the crack may be blunted. This toughening-optimal interfacial failure mode must contend with the mode of uninterrupted crack propagation into the reinforcement. Therefore, finding the conditions that allow the interfacial failure mode while suppressing the unwanted crack penetration has received a great deal of attention [10, 11]. Table 1 summarizes the several formulations of this topic, which is likely the main reason why no consensus has been established thus far. Criteria for reinforcement and interface fracture, apart from small variations in model geometry, are the main point of contention.

According to authors [12], the interface fracture is controlled by the cleavage stress (σi) produced by the approaching matrix crack (i.e., the tensile stress perpendicular to the interface) against the corresponding interfacial strength (σi,m). Similarly, the reinforcement fracture is governed by splitting stress (σr) (i.e., the tensile stress perpendicular to the matrix crack plane) against the corresponding strength (σr,m). They deduced that the interfacial failure mode will be activated if σi reaches σi,m before σr rises to σr,m based on these assumptions. On the other hand, authors [13, 14] looked at the energy release rate (Gi) for an extremely tiny crack expansion at the interface and Gr for an extremely tiny crack growth in the reinforcement. The interfacial failure mechanism was suggested as being activated by an energy-based situation, wherein Gi attains the interfacial toughness, Γi, prior to Gr reaching the reinforcement's toughness, Γr. Furthermore, authors [15] looked for a way to bring the two kinds of fracture criteria together by presuming that cohesive principles regulate both the interface failure and the reinforcement.

First, although faults of finite size are prevalent, the majority of current models make the assumption that the interface and reinforcement are defect-free or contain defects of an infinitesimally small size. Unphysical interpretations, such as the existence of infinite or nonexistent energetic driving factors for fracture initiation, could result from making such assumptions. Secondly, the stress state at the interface is affected by the residual stress that is generated during fabrication, al-

Table 1: Models of initiation of interfacial failure.

Model geometry		Fracture criteria	
An elliptical crack	Approaching a perfect bi-material interface	At normal incidence	Stress ratio
A sharp crack	Approaching a bi-material interface with pre-existing defects	At normal incidence	Energy release rate ratio
A sharp crack	Approaching a bi-material interface with pre-existing defects	At normal incidence	Energy release rate ratio and cohesive law
A sharp crack	Approaching/impinging on a perfect bi-material interface	At normal incidence	Energetic incremental condition
A sharp crack	Impinging on a perfect bi-material interface	At normal incidence	Energy release rate ratio
A sharp crack	Impinging on a perfect bi-material interface	At normal incidence	Stress ratio
A sharp crack	Impinging on a perfect bi-material interface	At normal incidence	Cohesive law
A sharp crack	Impinging on a perfect bi-material interface	At normal incidence	Energy release rate ratio

though this aspect has received less attention. For instance, if the interface is subjected to significant compressive residual stresses, it may prevent mode I fracture initiation, such as interfacial delamination.

Since the matrix/reinforcement interface is expected to dissipate far more energy than the brittle reinforcement itself, we have only covered the commencement of the favorable interfacial failure mode in fiber-reinforced composites so far. On the other hand, if the reinforcement breaks or comes loose from the matrix entirely, it can disrupt the interfacial failure mode after initiation. In order to accurately evaluate the energy dissipation capacity of each matrix/reinforcement interface, it is necessary to provide a detailed description of the interfacial failure process, beginning with its commencement and ending with its termination. In order to measure the improvement in total fracture toughness, it is necessary to take into account not only the individual interactions between the interfaces and reinforcements, but also their collective behavior.

According to authors [16, 17], there are two main processes that occur during the interfacial failure mode: first, there is interfacial debonding, and then the reinforcement is pulled out along the interface due to friction. Energy is dissipated during debonding by breaking the link between the matrix and reinforcement, and again during pull-out by frictional sliding at the interface. According to authors, there is a critical length (lc) of fiber reinforcement that, if not surpassed, prevents the reinforcement from breaking and keeps the interfacial failure mode going until pull-out is complete. According to his additional research, the relationship between the interfacial frictional stress (τf) and the reinforcement's fracture strength (σr,m) is approximately proportional to lc. For each given interface, this lc establishes a maximum allowable debonding energy dissipation (Wd) and pull-out energy dissipation (Wp). It is generally accepted that Wp is substantially larger than Wd, meaning that the bulk of the interface's energy dissipation capacity, W should be attributed to the frictional pull-out process. When reinforcements are reduced in magnitude, however, the validity of this reasoning remains debatable.

To find the work of fracture per unit area of the composite, the contribution of each fiber by the area density of fibers, assuming that each fiber fractures independently and exhibits identical properties. This allowed him to bridge the gap between the toughening effect of an assembly of fibers and that of an individual interface. By considering the statistical character of composites, expanded upon Kelly's findings. Take note that the work of fracture has been thought of as a fair indicator of fracture resistance, even though it is not exactly the same as fracture toughness. More complex models, like the discontinuous crack-bridging model, are needed for direct prediction of the improved fracture toughness of composites [18]. To keep things simple, we shall estimate composite fracture toughness using the work-of-fracture method.

Toughening in graphene nanomaterial-reinforced composites

Our review of the toughening mechanism in carbon fiber-reinforced plastic reveals that the current theoretical and computational models are severely lacking. From the beginning to the end of the interfacial failure process-which includes debonding and pull-out—no one knows what causes it. Even when we use the current models to describe composites reinforced with graphene nanomaterial, these problems remain. Consequently, a more comprehensive model of interfacial failure must be developed.

Note that nano-reinforcements are typically scattered throughout the matrix and don't provide a thick enough wall to prevent a matrix crack from penetrating the composite. So, in a loaded composite, a few platelet-like nano-reinforcements typically bridge a barely opened cleavage crack (Figure 1a). The cleavage surfaces are able to elude all of these platelets. A modified graphene model is shown in figure 1b since, because of the sparse dispersion, Kelly's assumption that each reinforcement behaves separately remains a fair approximation figure 1c. Figure 1c and the half model in figure 2a show that the relative interfacial displacement between the matrix and the reinforcement is driven by the increase in crack opening, Δ, which results from consecutive loading.

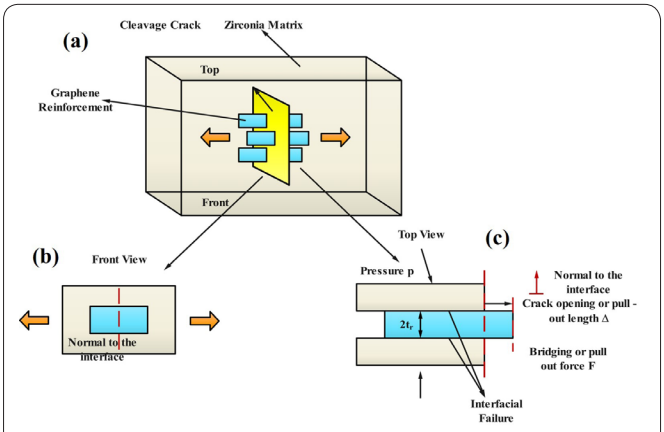


Figure 1: Fracture of a composite reinforced with graphene nanomaterials. **(a)** This work investigated a common case where scattered platelet-like nano-reinforcements bridge a cleavage crack. **(b)** The reduced graphene model in is the result of assuming that each reinforcement behaves individually. **(c)**The interfacial failure process is driven by the extraction of reinforcement from the matrix and the consequent rise in crack opening, Δ, caused by the loading.

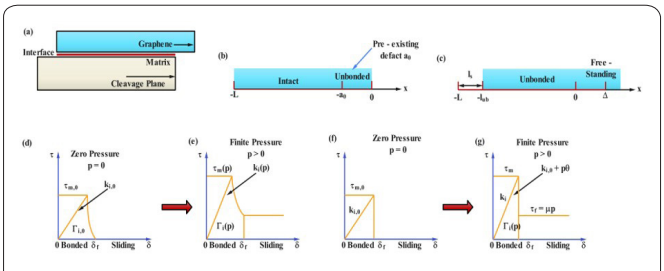


Figure 2: A shear-lag model that uses cohesive-frictional theory. **(a)** One reinforcement-matrix interface is taken into consideration by the half-reinforcement model. It is the pull-out length Δ, and the pull-out force, F, that cause the matching matrix/reinforcement interface to fail. **(b)** Initial configuration of the interface. **(c)** Final debonding of the interface and subsequent pull-out. **(d - g)** When describing the pressure-dependent sliding responses between the reinforcement and the matrix, an extended cohesive model is used, which includes the Coulomb friction model.

We simplify the situation by assuming that there is already a pre-existing defect at the interface, which is an unbonded segment of size a0, sitting near to the cleavage crack, and that the rest of the interface is initially whole (Figure 2b). The frictional force, τf, increases in the unbonded region as Δ grows, which delays the onset of debonding in the bonded region. This is followed by a redistribution of interfacial shear stress, τ, during the subsequent debonding. As seen in figure 2c, if the reinforcement strength is high enough, the entire contact can become unbonded and merely affected by friction. In most cases, the pressure applied to the interface, denoted as p, should determine the frictional force, τf. The assumption is that the Coulomb model is linear, with τf = μp, where μ is the friction coefficient. It is also believed that the pressure is evenly distributed, which will prevent interfacial delamination and provide proper reinforcement-matrix contact. The matrix-reinforcement bond's mechanical characteristics have a significant impact on the interfacial shear stress distribution. One way to describe the bonding qualities is using a cohesive model, which shows in figure 2d to 2g the relationship between the shear stress (τ) and the relative displacement (δ) at the interface. Chemical (e.g., covalent, hydrogen, or dangling bonds) and mechanical (e.g., mechanical locking owing to surface roughness) methods are usually used to accomplish the interfacial bonding [19]. The intricate process of bonding between surfaces, together with changes in surface pressure, leads to a broad spectrum of surface stiffness, ki, surface strength, τm, surface debonding length, δf, surface fracture energy, Γi, and surface frictional force, τf (Figure 2d and 2e). The micron-scale *in-situ* pull-out experiments performed were used to measure the unpressurized interfacial properties between a hexagonal boron nitride nanosheet (h-BN) and a zirconia (PDZ) substrate derived from polymer. The results showed that ki,0 ≈5.7 GPa/μm, τm,0 ≈66.4 MPa, δf ≈τm,0/ki,0, and œi,0 ≈0.5τmδf. The characteristics of the graphite/epoxy interface were investigated in millimeter-scale push-out experiments conducted. They found ki ≈0.2 MPa/μm and τm ≈1 - 7 MPa. The interface between a concrete slab and a cast-in-place concrete topping using meter-scale push-off experiments. The results showed that ki was around 3 - 19 kPa/μm and τm was about 0.2 MPa. The results show that the bonding between the surfaces of composites is multi-scale. Graphene nanomaterial-reinforced composites are best described by the length-scale of the h-BN/PDZ experiments, such as the interfacial shearing distance and the interfacial length. Using these data, we construct an extended cohesive model (Figure 2f and 2g) to describe the interfacial failure mechanism. The cohesive model exhibits a pressure-dependent stiffness, k_i=k_(i,0)+ pθ, a subsequent abrupt debonding at δ=δ_f, and the frictional sliding dictated by τ_f=μp. Further properties include a linear τ-δ response. Therefore, the shear strength, τ_m=τ_(m,0) + pθδ_f, is also pressure dependent. Keep in mind that there might be a gradual softening regime after τ approaches τ_m in the extended model and the h-BN/PDZ data, but it is not seen in figure 2d and 2e specifically. In addition, this expanded model is comparable to the slip-weakening model in earthquake mechanics, although it has not been applied to composites research.

According to the cohesive-frictional model mentioned earlier, a well-defined shear-lag problem is what defines the interfacial failure process (Figure 2). One half of the length of the matching reinforcement is the length of the contact under consideration, denoted as L. It is reasonable to concentrate on the reinforcement's deformation along its pull-out direction (the X-direction in figure 2) and assume the matrix is rigid because the Young's moduli of the matrix and graphene are typically within the same order of magnitude and the reinforcements are significantly thinner than their spacings. This ensures that the reinforcement's strain and stress distributions are nearly constant over its thickness. We anticipate small strains because the brittle reinforcement is not very stretchy. At the contact, however, the relative displacement might not be negligible, particularly during the sliding phase. In the deformed reinforcement, the relative displacement field, u(x), and stress field, σ(x), are linked along the X-direction through:

$$\sigma = E_r \mathrm{d}u/\mathrm{d}x \tag{1}$$

Where, E_r denotes the graphene's modulus. The variation in σ is caused by the interfacial shear stress.

$$\mathrm{d}\sigma/\mathrm{d}x = \tau/t_r \tag{2}$$

Where, t_r represents the graphene's half-thickness. The distorted configuration defines both $a(x)$ and $\sigma(x)$. Equation 1 and equation 2 when combined yield:

$$\mathrm{d}^2u/\mathrm{d}x^2 = \tau/(Et_r) \tag{3}$$

The length of the contact interface reduces by l_s with an initial length of L, as the pull-out length Δ rises. Hence, the left end of the reinforcement travels in the direction of u($l_s - L = J_s$) and in the absence of stress, $\sigma(l_s - L = 0)$.

The interface is composed of an unbonded/sliding region ($-l$ub < x < 0) with a length of $l$ub a bonded region ($l_s - L < x < -l_{ub}$) with a length of lb = $L - l_s - l_{ub}$) and a freestanding region (0 < x < Δ) with a length Δ. The relative displacement of δ_f at $x = -l_{ub}$ is maintained by the increasing unbonded area, where $u(-l_{ub}) = \delta_f$. Interfacial shear stress distribution as shown in figure 2g by the cohesive-frictional law is as follows:

$$\tau = \begin{cases} k_i u, & l_s - L \le x \le -l_{ub} \\ \tau_f, & -l_{ub} \le x < 0 \\ 0, & 0 \le x \le \Delta \end{cases} \tag{4}$$

Equivalent equation 3 and equation 4 are substituted to obtain a piecewise controlling equation:

$$\mathrm{d}^2u/\mathrm{d}x^2 = \begin{cases} u/l_0^2, & l_s - L \le x < -l_{ub} \\ \tau_f/(Et_r), & -l_{ub} \le x < 0 \\ 0, & 0 \le x \le \Delta \end{cases} \tag{5}$$

This is where the characteristic length $l_0 = \sqrt{E_r t_r / k_i}$ measures the local distribution of the interfacial shear stress in the bonded portion of the interface. So, it calculates an approximation for the size of the debonding "process zone" (PZ) where the interfacial bonds are considerably more distorted than outside. While interfacial stiffness decreases as reinforcement stiffness rises, PZ size grows as reinforcement stiffness

increases. Taking into account the boundary conditions and continuity conditions for displacement and stress described before allows one to solve the differential equation in equation 5. We have $l_s - L \le x \le -l_{ub}$.

$$u = \delta_f \frac{\cosh\left[\left(x + L - l_s\right)/l_0\right]}{\cosh\left[l_b/l_0\right]} \tag{6}$$

There is a correlation between, *l*-b and *l*-ub, because the displacement at the left end of the bonded region is $l_s = \delta_{fsech}\left(l_b/l_0\right) \le \delta_f$.

$$l_{ub} = L - l_b - \delta_f \operatorname{sech}\frac{l_b}{l_0} \tag{7}$$

Applying equation 1, we can determine the stress at the junction of the bonded and unboned areas, which gives:

$$\sigma\left(-l_{ub}\right) = \frac{E_r \delta_f}{l_0}\tanh\frac{l_b}{l_0} \tag{8}$$

For $-l_{ub} \le x \le 0$, we have:

$$u = \delta_f + \frac{\tau_f}{2k_i l_0^2}\left(x + l_{ub}\right)\left(x + l_{ub} + l_0\frac{2\tau_m}{\tau_f}\tanh\frac{l_b}{l_0}\right) \tag{9}$$

The displacement at $x = 0$ is precisely equal to the initial length of the free-standing portion of the reinforcement, which ranges from $(0 \le x \le 0)$.

$$u\left(0\right) = \delta_f + \frac{\tau_f}{2k_i l_0^2} l_{ub}\left(l_{ub} + l_0\frac{2\tau_m}{\tau_f}\tanh\frac{l_b}{l_0}\right) \tag{10}$$

Equal to the continuous stress at the junction of the free-standing and unbonded sections is the stress in the free-standing part:

$$\sigma = \sigma\left(0\right) = \frac{E_r}{k_i l_0^2}\left(\tau_f l_{ub} + \tau_m l_0 \tanh\frac{l_b}{l_0}\right) \tag{11}$$

Extending the reinforcing by σ/*E*r. Thus, the pull-out length, Δ, and force F, can be solved semi-analytically:

$$\Delta = u\left(0\right)\left(1 + \frac{\sigma\left(0\right)}{E_r}\right)$$

$$= \left(\frac{\tau_f l_{ub}^2}{2k_i l_0^2} + \frac{\delta_f l_{ub}}{l_0}\tanh\frac{l_b}{l_0} + \delta_f\right)\left(1 + \frac{\tau_f l_{ub}}{k_i l_0^2} + \frac{\delta_f}{l_0}\tanh\frac{l_b}{l_0}\right) \tag{12}$$

$$F = \sigma\left(0\right).w_r.2t_r = 2w_r\left[\tau_f l_{ub} + \tau_m l_0 \tanh\frac{l_b}{l_0}\right] \tag{13}$$

Where wr denotes the graphene's width (in the out-of-plane direction of the shear-lag model). The reinforcement is loaded on both sides, as seen in figure 1c and figure 2a, and this is explained by the two-digit pre-factor in equation 13. The crucial pull-out force, Finit, needed to start the debonding process from a size a0 defect can be easily determined by substituting $l_{ub} = a_0 - \delta_f$ in equation 13 instead of l_{ub}.

It is important to remember that the debonding process under consideration encompasses the whole procedure, beginning with the failure of the most strained link and continuing until all of the bonds at the interface have failed. Thus, it could not be a simple debonding process, but rather a hybrid of the two, including frictional sliding and debonding in the bonded area (in the unbounded region). These two physically separate processes are highly related and should not be treated independently, according to earlier research [20].

While debonding is a complex process, the pull-out that follows is based entirely on frictional sliding. The pull-out force, F, is thus directly related to the contact interface length, $l_{ub} = L - l_s$, and it falls monotonically as Δ approaches Δ = L.

$$F = 2w_r\tau_f l_{ub} \tag{14}$$

The interfacial displacement field is controlled when there is no bonded area.

$$d^2u/dx^2 = \begin{cases} \tau_f/\left(Et_r\right), & -l_{ub} \le x < 0 \\ 0, & 0 \le x \le \Delta \end{cases} \tag{15}$$

For $-l_{ub} \le x \le 0$, we have:

$$u = \frac{\tau_f}{2k_i l_0^2}\left(x + l_{ub}\right)^2 + L - l_{ub}, \quad \sigma = \frac{\tau_f}{k_i l_0^2}\left(x + l_{ub}\right) \tag{16}$$

At $x = L - l_{ub}$, fulfilling the stress-free condition. That being said, the pull-out length can be calculated using the same method as equation 12:

$$\Delta = u\left(0\right)\left(1 + \frac{\sigma\left(0\right)}{E_r}\right) = \left(\frac{\tau_f l_{ub}^2}{2k_i l_0^2} + L - l_{ub}\right)\left(1 + \frac{\tau_f l_{ub}}{k_i l_0^2}\right) \tag{17}$$

The changes in F and Δ as the interfacial failure progresses under various pressures are illustrated in figure 3a. Assuming $\mu = \theta\delta_f = 0.2$, the interface starts with a length of 100.0 μm and has a pre-existing defect of size a0 = 10.0 μm. Table 2 lists all the additional factors. Figure 3a and its insets show the F-Δ curve, which shows the change from debonding to pure frictional pull-out. The only process that produces a nonzero F in the absence of friction and pressure is debonding. Due to its simple linear relationship, the F-Δ curve that exists before debonding begins is not displayed.

Debonding and the initial stage of frictional pull-out are magnified in figure 3b and 3c, respectively, revealing substantial variation for various values of L and p. The significance of pre-existing flaws in starting the debonding process is shown by the fact that the initiation point, denoted by crosses, is affected by the initial defect size, a0. Fascinatingly, one master curve that is unaffected by a0 represents the later evolution of F and Δ. The "snap-back" instability, shown by dashed arrows in figure 3b and 3c as well as the insets of figure 3a, is a notable aspect of these F-Δ curves. It occurs at the end of the debonding process, when Δ = Δend, and debonding can only continue in a quasi-static way if F and Δ decrease at the same time. The interface's shrinkage and debonding reduce its load-carrying capabilities, which is accounted for by the fall in F, while the elastic recovery of the stretched reinforcement causes the decrease in Δ. In a system that is consistently loaded, the instability point is usually not reached. Instead, the interface becomes totally unbonded as Δ beyond Δend, and the system transitions to pure sliding. The debonding and pull-out

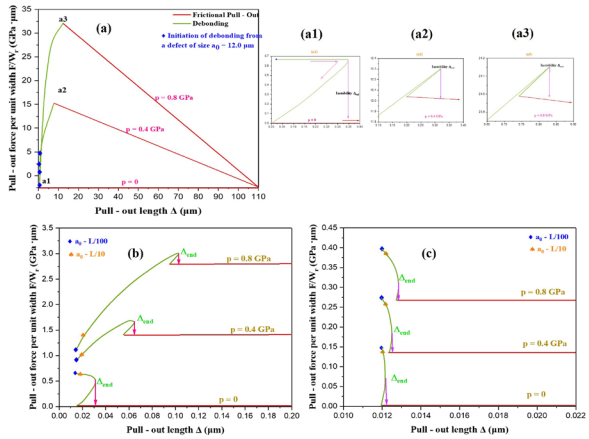


Figure 3: Development of the pull-out force as a function of time during interface failure. There is an accounting for both the debonding and pull-out processes. **(a)** The full progression of F, starting from the start of debonding and ending with the pull-out process, for a length of L = 100 μm. Using p = 0, 0.4 GPa, and 0.8 GPa, the insets **(a1** to **a3)** show a universal "snap-back" instability as the transition from debonding to frictional pull-out (marked in dashed arrows). **(b** and **c)** The evolution of F during the debonding and early pull-out stages for L = 10 μm and L = 1 μm may be observed in a zoomed-in image.

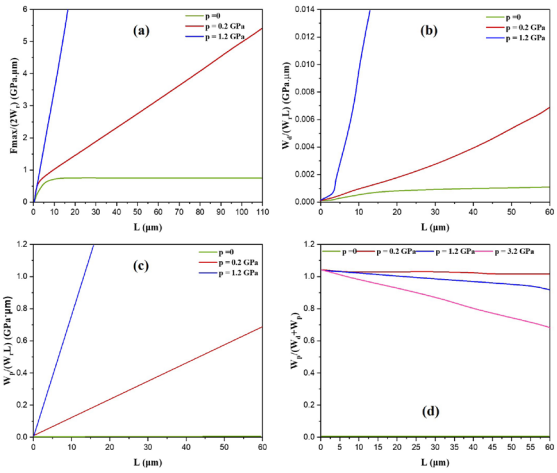


Figure 4: Interfacial failure process essential characteristic quantities. **(a)** The strongest force that can be applied to separate two surfaces before they fail completely. **(b)** The quantity of energy lost during debonding. **(c)** The quantity of energy lost during the extraction procedure. **(d)** The pull-out process's relative contribution to energy dissipation.

processes are both initiated simultaneously by the "snap-back" instability.

The pull-out force, F, reaches a plateau for long interfaces (L = 100.0 μm) right after debonding starts (Δ = Δinit), while it drops significantly for shorter interfaces (L = 1.0 and 10.0 μm). According to authors [21], the size of the PZ, l0 (refer to equation 5), controls this transition. In contrast, F is more affected by changes throughout the length of the bonded region when an interface, ($L \approx l_0$ or $L < l_0$) experiences shear stress that is more dispersedly distributed in the bonded region. The highest pull-out force, F_{max}, also reflects the difference between these two modes. As shown in figure 4a for the pressure-free scenario, when L is small, F_{max}. grows approximately linear with L. The reason behind this is that the interfacial shear stress is almost evenly distributed, with ($\tau \approx \tau_m$) and L restricting the maximum value of F. (i.e., the so-called strength-governed limit). A constant F can drive the energetic fracture process of debonding a long contact, however this process becomes saturated when $L >> l_0$ (i.e., the so-called energy-governed limit).

Because of friction, the plateau of F for $L >> l_0$ in the pressure-free case disappears for finite pressures, and F could even go up when debonding is going on. F_{max}, which may be attained either halfway through or at the end of the debonding process, is hence not always equal to Finit. When the contact is long, the pressure effect is stronger, and friction, not interfacial bonding, is the dominant source of the maximum force (F_{max}), which is approximately proportional to L (Figure 4a).

Both the debonding (Wd) and pull-out (Wp) energies dissipated by an interface as a function of L and p are illustrated in figure 4b and 4c, respectively. The integral of F/2 from Δinit to Δend is a convenient way to assess Wd, while the integral of F/2 from Δend to L is the best way to evaluate Wp. All of the curves in figure 4 assume of a modest defect size, a0 = L/100. Although Wp grows linearly with L, the Wd-L relationship is more complicated and defies simple power law description, unlike Kelly's theory [22]. We plot the ratio of Wd to W (= Wd + Wp) for various values of L and p in figure 4d to understand the relative contributions to energy dissipation by the debonding and pull-out processes. Despite the common belief that W ≈ Wp, a significant amount of energy can be lost during debonding. The pressure-free scenario, where Wp = 0 and Wd > 0, is not the only one where this variation occurs. Given that Wd is the product of linked debonding in the bound zone and frictional sliding in the unbounded region, it follows that for big enough p and L, Wd can also be similar to Wp. The proportion contribution from Wd grows as p increases from 0.2 GPa to 3.2 GPa, as seen by the curves in figure 4d. An increasing Δend/L with p is shown in figure 3, which is a result of the shortened pull-out process and the extended debonding process.

Theoretically, an interface's ability to dissipate energy should be similar to $\tilde{W} = \tau_f L^2/2 + \Gamma_i L$ which is the total of the energy dissipation caused by a rigid reinforcement's unbounded interface and a bonded but frictionless interface. As a result, in figure 5a, we show the relationship between W and $\tilde{W}$ as a function of L for various pressure types.

Interestingly, these curves all show a nonmonotonic dependence on p and monotonically rise with L. When considering the size-induced differences in mechanical characteristics, there is a notable difference between W and $\tilde{W}$ for small L, suggesting that short reinforcements may not be the best option for dissipating energy. The energy dissipation capacity of the reinforcements, W, should be enhanced by applying a bigger pressure, since $\tilde{W}$ grows with p. The failure of the reinforcements themselves is a limiting factor that prevents them from reaching their toughening potential; this issue has attracted a lot of attention from researchers but is beyond the scope of this work [23]. Here, we will assume an effective strength, S, that governs their failure for the sake of simplicity.

Accordingly, dissipation must proceed without interruption.

$$F_{max} \leq S.2t_r \quad (18)$$

The grey walls and arrows in figure 5b indicate the "admissible" p-L regime that equation 18 finds for a particular S.

Finding the optimal/maximum L for a given p or an optimal/maximum p for a given L is as simple as looking at the intersection line between the boundary of the acceptable regime and the contour plot of W (see the lines in figure 5b). We can make some broad observations despite the fact that figure 5b is model parameter dependent (Table 2):

- Combining a big L with a little p on the junction line is advantageous. There is a trade-off between big L and p, which can both increase W, due to the constraint in equation 18. In order to achieve higher toughness, it is more important to enhance L.
- Reinforcements have less of an impact on toughness after L reaches a certain upper bound (caused by practical constraints like manufacture) and an optimal p is reached.
- Because a lengthy interface is more likely to fracture, an upper limit of L is determined by a lower bound of p, as shown in equation 18. When it comes to toughening composites, a large S is always a good thing. Because of their exceptional strength, graphene nanoparticles are a natural choice for use in composite design.

Results and Discussion

This model decouples the dissipation of energy during debonding and pull-out and emphasizes the roles played by interfacial pressure (p) and interface length (L). We found two important parameters that characterize the interfacial failure mechanism: the total energy dissipation capacity of the interface (W) and the maximum pull-out force (F_{max}). The maximum allowable design space for p and L, where the interfacial failure process can start and continue unimpeded (Equation 18), is defined by F_{max} and the reinforcing strength, S. A moreack deflection problem has been extensively explored in the literature, but a more practically relevant topic is maintaining an uninterrupted interfacial failure mode in composites (Table 1).

Figure 3c shows that prior research is lacking since it failed to account for the sensitivity to pre-existing flaws and pressure, even in the strength-governed limit (i.e., tiny L) where F_{max} = Finit. Consideration of all constraints is necessary to maximize W in real-world scenarios, since some restrictions may not be addressed by equation 18 (Figure 5b). The work-of-fracture technique allows us to roughly estimate the overall toughness improvement of the composites as 4 nW, assuming n aligned bridging reinforcements (with length 2L and thickness $2t_r$) per unit area. So, improving toughness and W are the same thing. In this work, we concentrate on the toughening effects for one specific fracture mode/direction, although it is important to mention that the mechanical properties of the composites are anisotropic due to the alignment of the reinforcements. In real-world scenarios, anisotropy of toughening might be especially attractive when one direction of loading requires substantially stronger toughening than the others.

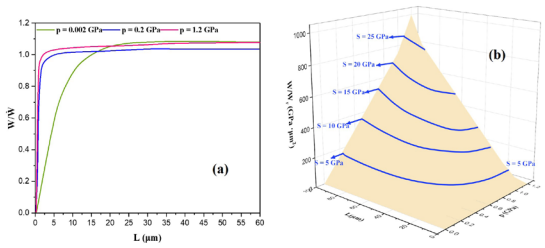


Figure 5: Maximizing the matrix/reinforcement interface's ability to dissipate energy. **(a)** Increases in energy dissipation are often associated with long interfaces and high pressures. **(b)** However, the dissipation capacity can only be used in theory due to the reinforcement's failure strength, S. As indicated by the arrows and the grey walls, the permissible design space that avoids the intermediate interruption of the interfacial failure process is defined by the p-L regime. The best value of L for a certain value of p (or the best value of p for a particular value of L) is defined by the intersecting line between the acceptable regime boundary and the contour plot of W.

Table 2: Model parameters utilized for this research.

E_r (GPa)	500.0
t_r (μm)	0.2
$\tau_{m,0}$ (MPa)	66.4
$k_{i,0}$ (GPa/μm)	5.7
δ_r (μm)	0.0116

This study's continuum analysis failed to detect a size-dependent change in the toughening mechanism. The usage of graphene nano-reinforcements appears to provide minimal benefits, according to this result. It should be noted that factors such reinforcing stretchability and interfacial properties might show a strong size-dependence, yet our theoretical paradigm is applicable to both micro- and nano-platelets. One example is the employment of longer reinforcements made possible by nanomaterials' great strength (i.e., a reinforcement material with larger L that does not undergo fracture). Because graphene nano-platelets are thinner than conventional ones, there are more matrix/reinforcement contacts per unit volume, which boosts toughness. In addition, since the interface and bulk/interfacial properties are not easily observable experimentally, the continuous analysis makes it difficult to characterize them when each thin reinforcement is located within several atomic spacings from the interface.

Conclusion

The assumption that the matrix/reinforcement contact is subject to a cohesive-frictional law that governs debonding and frictional sliding forms the basis of our work. In order to build robust ZMCs for a particular material system, it is crucial to accurately characterize the interface, paying close attention to the size and pressure effects. Engineered interfacial bonding and morphology provide new possibilities for controlling interfacial properties, made possible by graphene nanomaterials' distinctive layered structure. Aside from the "sword-in-sheath" manner of fracture bridging seen with multiwalled carbon nanotubes, other failure modes may emerge because of the weak connection between the interior layers of graphene nanomaterials. Debonding and pull-out may not

happen at the matrix/reinforcement contact but rather between the interior layers of the nano-reinforcements. These two processes can work together to increase toughness in ways linked to differences in the particular reinforcement structures and characteristics.

When applying the cohesive frictional rule in practice, it is also important to think about where the pressure is coming from. The thermal expansion mismatch between the matrix and reinforcements causes most composites to have substantial residual stresses. Furthermore, significant pressure at the interface can be exerted by external loading. This may have similarities to how T-stress affects composite fracture.

Acknowledgements

None.

Conflict of Interest

None.

References

1. Viet NV, Kuo WS. 2012. Shear transfer in fractured carbon nanotubes under torsion. *Mater Sci Eng A* 536: 256-264. https://doi.org/10.1016/j.msea.2012.01.009
2. Guo G, Zhu Y. 2015. Cohesive-shear-lag modeling of interfacial stress transfer between a monolayer graphene and a polymer substrate. *J Appl Mech* 82(3): 031005. https://doi.org/10.1115/1.4029635
3. Viet NV, Kuo WS. 2012. Load transfer in fractured carbon nanotubes under tension. *Compos Part B Eng* 43(2): 332-339. https://doi.org/10.1016/j.compositesb.2011.06.007
4. Gholami R, Khoramishad H, da Silva LF. 2020. Glass fiber-reinforced polymer nanocomposite adhesive joints reinforced with aligned carbon nanofillers. *Compos Struct* 253: 112814. https://doi.org/10.1016/j.compstruct.2020.112814
5. Uddin MN, Huang ZD, Mai YW, Kim JK. 2014. Tensile and tearing fracture properties of graphene oxide papers intercalated with carbon nanotubes. *Carbon* 77: 481-491. https://doi.org/10.1016/j.carbon.2014.05.053
6. Roy S, Akepati A. 2014. Multi-scale modeling of fracture properties for nano-particle reinforced polymers using atomistic J-integral. In ASME International Mechanical Engineering Congress and Exposition, Montreal, Quebec, Canada.
7. Lazarova R, Mourdjeva Y, Nihtianova D, Stefanov G, Petkov V. 2022. Fabrication and characterization of aluminum-graphene nano-platelets—nano-sized Al_4C_3 composite. *Metals* 12(12): 2057. https://doi.org/10.3390/met12122057
8. Hess P. 2015. Graphene as a model system for 2D fracture behavior of perfect and defective solids. *Frat Integr Strut* 9(34): 341-346. https://doi.org/10.3221/IGF-ESIS.34.37
9. Robinson MJ, Adams TC. 2020. Performance of FRP composite lap joints utilizing fiber tow steering. *Compos Part B Eng* 190: 107910. https://doi.org/10.1016/j.compositesb.2020.107910
10. Pedrazzoli D, Kravchenko OG, Manas-Zloczower I. 2016. Interlaminar fracture toughness of woven glass fiber-epoxy laminates with carbon nanotube buckypapers. In Proceedings of Annual Technical Conference, Indianapolis, USA.
11. Guest J, Kinloch IA, Young RJ. 2023. The role of filler aspect ratio in the reinforcement of an epoxy resin with graphene nanoplatelets. *J Mater Sci* 58(23): 9473-9485. https://doi.org/10.1007/s10853-023-08603-3
12. Davoudi K. 2017. Temperature dependence of the yield strength of aluminum thin films: multiscale modeling approach. *Scripta Mater* 131: 63-66. https://doi.org/10.1016/j.scriptamat.2016.12.039
13. Javanmard Sistani A, Shariati M, Zamani P, da Silva LF. 2023. Mode-I and II fracture behavior of metal-to-composite bonded interfaces with a graphene nanoplatelet-reinforced structural epoxy adhesive. *Proc Inst Mech Eng Part L J Mater Des Appl* 1-6. https://doi.org/10.1177/14644207241226609
14. Nguyen MK. 2018. Atomistic simulation study of crack tip blunting and the influence of blunting behavior on the fracture strength of a single layer graphene sheet. In 4th International Conference on Green Technology and Sustainable Development, Ho Chi Minh City, Vietnam.
15. Fattahi AM, Mondali M. 2014. Theoretical study of stress transfer in platelet reinforced composites. *J Theor Appl Mech* 52(1): 3-14.
16. Khoei MA, Darvizeh A, Sadeghi H, Maghrour A, Darvizeh A. 2022. A scaled framework for analysis of crack propagation in teeth using equivalent inorganic materials. *Proc Inst Mech Eng Part C J Mech Eng Sci* 236(14): 7593-7616. https://doi.org/10.1177/09544062221079502
17. McClenny LD, Butt MI, Abdoelatef MG, Pate MJ, Yee KL, et al. 2022. Experimentally validated multiphysics modeling of fracture induced by thermal shocks in sintered UO_2 pellets. *J Nucl Mater* 565: 153719. https://doi.org/10.1016/j.jnucmat.2022.153719
18. Izadifar M, Thissen P, Abadi R, Jam AN, Gohari S, et al. 2019. Fracture toughness of various percentage of doping of boron atoms on the mechanical properties of polycrystalline graphene: a molecular dynamics study. *Phys E Low Dimens Syst Nanostruct* 114: 113614. https://doi.org/10.1016/j.physe.2019.113614
19. Dyck A, Wicht D, Kauffmann A, Heilmaier M, Böhlke T. 2023. Revisiting analytic shear-lag models for predicting creep in composite materials. *Scripta Mater* 224: 115142. https://doi.org/10.1016/j.scriptamat.2022.115142
20. Wen F, Shan S, Radecki R, Staszewski WJ, Cheng L. 2021. Shear-lag modelling of surface-bonded magnetostrictive transducers for shear horizontal wave generation in a non-ferromagnetic plate. *Smart Mater Struct* 30(3): 035026. https://doi.org/10.1088/1361-665X/abe183
21. Jian Y, Zhang T, Wang X, Kyaw L, Pow EHN, et al. 2022. Effect of supporting dies' mechanical properties on fracture behavior of monolithic zirconia molar crowns. *Dent Mater J* 41(2): 249-255. https://doi.org/10.4012/dmj.2021-090
22. Sandoz-Rosado E, Beaudet TD, Balu R, Wetzel ED. 2016. Designing molecular structure to achieve ductile fracture behavior in a stiff and strong 2D polymer, "graphylene". *Nanoscale* 8(21): 10947-10955. https://doi.org/10.1039/c5nr07742g
23. Rabel K, Nold J, Pehlke D, Shen J, Abram A, et al. 2022. Zirconia fixed dental prostheses fabricated by 3D gel deposition show higher fracture strength than conventionally milled counterparts. *J Mech Behav Biomed Mater* 135: 105456. https://doi.org/10.1016/j.jmbbm.2022.105456